

Quantitative modeling of regular retinal microglia distribution

Yoshie Endo¹, Daisuke Asanuma², Shigeyuki Namiki², Kenzo Hirose², Akiyoshi Uemura³, Yoshiaki Kubota⁴, Takashi Miura^{1*}

1 Department of anatomy and cell biology, Graduate School of Medical Sciences, Kyushu University, Fukuoka, Japan

2 Department of Pharmacology, Graduate School of Medicine, The University of Tokyo, Tokyo, Japan

3 Department of Retinal Vascular Biology, Nagoya City University Graduate School of Medical Sciences, Japan

4 Department of Anatomy, Keio University School of Medicine, Tokyo, Japan

- *Corresponding author: Takashi Miura

Department of Anatomy and Cell Biology

Graduate School of Medical Sciences

3-1 Maidashi Higashi-ku

Fukuoka, 8120054, Japan

Tel: +81-92-642-6048

E-mail:miura_t@anat1.med.kyushu-u.ac.jp

- Model of regular spacing of retinal microglia
- Keywords: retina, microglia, regular spacing, mathematical model

1 Abstract

Microglia are resident immune cells in the central nervous system (CNS), showing a regular distribution. Advancing microscopy and image processing techniques have contributed to elucidating microglia's morphology, dynamics, and distribution. However, the mechanism underlying the regular distribution of microglia remains to be elucidated.

First, we quantitatively confirmed the regularity of the distribution pattern of microglial soma. Second, we formulated a mathematical model that includes factors that may influence regular distribution. Next, we experimentally quantified the model parameters (cell movement, process formation, and ATP dynamics). The resulting model simulation from the measured parameters showed that direct cell-cell contact is most important in generating regular cell spacing. Finally, we tried to specify the molecular pathway responsible for the repulsion between neighboring microglia.

Author summary

Microglia are resident immune cells in the central nervous system. It is known that the microglia cells show a regular distribution, but the mechanism underlying the regular distribution remains to be elucidated. In the present study, we quantitatively assayed the regularity of the microglia soma distribution using the image processing technique. Next, we formulated a mathematical model of cell distribution that includes factors that may influence regular distribution. Next, we experimentally quantified the model parameters using organ culture. As a result, we obtained parameters for cell migration, cell process dynamics, and extracellular ATP dynamics. Then we undertook numerical simulation of the mathematical model using the parameters obtained by the experiments. The resulting model simulations showed that direct cell-cell contact is the most important factor in generating regular spacing. Finally, we screened possible molecular pathways involved in the regular spacing of microglia, which confirmed the validity of the model.

2 Introduction

Microglia are resident macrophages in the CNS and show a regular distribution ([1], Fig. 1A). Microglia cells have several physiological functions; control of neuronal cell

production, neural migration, axonal growth, synaptogenesis [2, 3] and angiogenesis [4].
Microglia cells also plays a role under pathological conditions; defense against infection,
inflammation, trauma, ischemia, tumor, and neurodegeneration [5]. Microglia have two
modes of action (Fig. 1B) - in the healthy brain, they are inactive (resting) and become
active during an immune response [6]. The resting and activated microglia have distinct
morphology (Fig. 1C). Resting microglia have a small soma and elongated ramified
processes extending and retracting continuously, surveying their microenvironment [7].
When microglia recognize a pathogen or other inflammatory stimulus, they rapidly
become an active state, retract their processes and become efficient mobile effector cells.
ATP mediates the chemotaxis toward the injured site. Injured cells release ATP,
activating the microglial P2X and P2Y receptors. Extracellular ATP regulates microglia
branch dynamics and mediates microglial movement toward the injury [8–10]. Local
injection of ATP can mimic this immediate chemotactic response [11].

Microglia are derived from primitive hematopoiesis progenitors in the fetal yolk sac
during the early embryonic stage [12, 13]. They migrate into all CNS regions, disseminate
through the brain parenchyma, and acquire a specific ramified morphological
phenotype [14]. Quail microglial precursors enter the retina from the optic nerve head
and migrate in a central to peripheral direction. ATP plays a role in the entry and
migration of microglial precursors into the developing quail retina. The mechanism for
microglial colonization of the CNS appears to be a conserved process across
vertebrates [15]. Other adult tissue-resident macrophages are Kupffer cells in the liver,
Langerhans cells in the epidermis, and alveolar macrophages in the lung [16].

Advancing microscopy and image processing techniques have made the assessment of
microglia morphology more feasible. Nimmerjahn *et al.* reported a highly active motile
processes of resting microglial cells using in vivo two-photon imaging [7]. Davis *et al.*
reported microglia density, nearest neighbor distance, regularity index, and phenotypes
such as soma size and roundness of the mouse retina [17]. However, the mechanism and
the molecular pathway of the regular distribution are unclear.

In the present study, we quantified the microglia distribution pattern and confirmed
the pattern regularity. Next, we formulated a mathematical model that includes the
known regulatory factors of microglial migration. To verify the models experimentally, we
quantified the model parameters, reproduced the dynamics with numerical simulations,

and tried to specify the molecular pathway responsible for the repulsion between neighboring microglia.

Fig 1. Microglia distribution and morphology. (A) Microglia in the peripheral avascular and the central vascular area of a P5 mouse retina. (B) Observation of activated microglia in the organ culture. A part of the resting microglia was converted to activated microglia and migrated to the injured peripheral edge during a 12-hour time-lapse assay of mouse retina organ culture. (C) Activated microglia stained with MAC2 after the organ culture.

3 Materials and methods

3.1 Tissue preparation

We used postnatal day five (P5) wild-type mice (Slc: ICR strain) purchased from Japan SLC, Inc., Japan. We sacrificed the P5 mice by decapitation and isolated eyeballs from the orbit for organ culture. After removing eyelids and fat tissues, we made a small hole at the cornea center with a 26G needle. The sclera was gradually removed from the hole using fine forceps, and we isolated the retina in Hanks' Balanced Salt Solution (HBSS). We removed the lens, vitreous body, and vitelline arteries and prepared the retina fragment with fine forceps. All the animal experiments were undertaken under the permission of the Kyushu University animal experiment committee (A29-036-1).

3.2 Immunohistochemistry

We performed immunohistochemistry (IHC) of whole-mount samples or tissue sections as previously described [18]. Eyes were fixed for 20 min in 4% paraformaldehyde (PFA) in phosphate-buffered saline and then dissected. Retinal cups were post-fixed for 30 min and then stained by a standard protocol.

Hamster anti-CD31 (1:1,000; 2H8; Chemicon, Temecula, CA), MAC2 (CEDARLANE), and Iba1 (1:1,000; WAKO, Osaka, Japan) were used as primary monoclonal antibody. For nuclear staining, we treated specimens with DAPI (Molecular Probes) or Hoechst 33342 (Dojindo).

3.3 Organ culture

We dissected P5 mouse retinas in HBSS(+). Retinal pieces were cultured on a cell culture insert with a 0.4 μm pore diameter (Millicell PICM0RG50, Merck Millipore Ltd, Cork, Ireland) in DMEM/Ham's F-12 without Phenol Red (Nacalai Tesque, INC. Kyoto, Japan) supplemented with 10% FBS and 1 % antibiotics (Penicillin-Streptomycin Mixed Solution, Nacalai Tesque, INC. Kyoto, Japan). We added Ib4 lectin (1/1000, Invitrogen I21411) to stain both resting and activated microglia.

Reagents used in the organ culture experiments are: Phosphatidylinositol-specific Phospholipase C from *Bacillus cereus* (PI-PLC, 0.5 U/ml, Sigma-Aldrich P5542), Recombinant Mouse sFRP-1 Protein (1 $\mu\text{g/ml}$, R&D Systems, MN9019-SF-025), Plexin-D1 Fc fragment (30 $\mu\text{g/ml}$), Alexa Fluor 647-ATP (5 μM , Invitrogen A22362), and Clopidogrel (25 μM , TOCRIS 249010).

3.4 Extracellular ATP dynamics

We quantified the ATP uptake and diffusion using Alexa Fluor 647-ATP (Invitrogen A22362). We added 5 μM of the fluorescently labeled ATP to the culture medium of the P5 retina organ culture. After 1 hour of incubation, we observed the ATP diffusion of the ATP using fluorescence recovery after photobleaching (FRAP). The diffusion coefficient is obtained according to [19]. ATP uptake by microglia was assessed by observation of the culture after 12 hours.

We observed the extracellular ATP concentration with ATPOS fluorescent sensor [20, 21]. Dissected P5 retina cups were washed in pH 7.4 HEPES buffer solution (HBS, 25 mM HEPES, 125 mM NaCl, 4 mM KCl, 2 mM CaCl₂ and 1 mM MgCl₂), and incubated for 5 minutes at room temperature in 100 μl of 0.33 μM neuronal-surface-targeted ATPOS, a molecular complex of ATPOS with BoNT/C-Hc and Alexa Fluor 488 (Alexa488) labeled-streptavidin [20, 21] with 1/100 IB4-DyLight649 (DL-1208-5, Vector Laboratories). Then, the retina cups were washed with HBS + 0.1% BSA three times and transferred on the slide glass of a glass-bottom dish (3911-035-IN, Iwaki Glass). After supplementing with 500 μl of DMEM/F-12 + 10 % FBS, the optic cups were dissected, and the retina's anterior half was observed using a Nikon A1 confocal microscope. Extracellular ATP distribution was estimated using the

Cy3/Alexa488 signal ratio [20]. We checked the fluorescence response of ATPOS in the organ culture by local application of 2 μ l of 10 mM adenylyl-imidodiphosphate (Sigma-Aldrich A2647) (AMP-PNP), an ATP analog that is not degraded by ATPase, as a positive control. The final concentration of AMP-PNP should be 10 μ M in the culture medium. The AMP-PNP concentration was calculated using a molar absorption coefficient of 15,000 /M/cm at 260 nm.

3.5 Image analysis

3.5.1 Evaluation of microglia morphology

We acquired the confocal images (30 μ m z-stack at 3 μ m intervals, Nikon A1, 20 \times objective) of the mouse retina. We performed the image processing using ImageJ (Fiji) software [22] (Fig. 2A). First, we created the maximum intensity projections of Z stacks, removed the noise by despeckling and smoothing, and obtained the binary images by thresholding. Since the skeleton length (microglia process) increased as the threshold values decreased, the threshold values were determined manually just before the skeleton length increased explosively (35.2 ± 0.84 , mean \pm SE).

Next, we obtained the distance map images and the skeleton images from the binary images. We calculated the process distribution using the skeleton images. We multiplied the distance map image and the skeleton image for the evaluation of microglia thickness. The mean gray value of the multiplication result represents the mean thickness including the soma and the processes.

3.5.2 Evaluation of microglia distribution

The Hopkins-Skellam index (HSI, [23]) was adapted to analyze cell soma distribution (Fig. 2B). HSI is calculated from the following equation:

$$HSI = \frac{\sum_{i=1}^N r_{1i}^2}{\sum_{i=1}^N r_{2i}^2}. \quad (1)$$

r_1 is a distance from a point chosen at random to its nearest individual, r_2 is a distance from an individual chosen at random to its nearest individual, and N is sample size.

$HSI < 1$, $HSI = 1$, $HSI > 1$ represents regular, random and aggregate patterns respectively (Fig. 2B).

Fig 2. Image Analysis. (A) Image processing for evaluation of microglia morphology and distribution. (B) HSI and regularity of the soma distribution.

3.6 Numerical simulations

All numerical simulations are implemented using *Mathematica* (Wolfram Research). The source code of the numerical simulation is provided as an electronic supplementary electronic material.

4 Results

4.1 Regular distribution of microglia in avascular and vascular area

We quantified the microglia soma distribution and the microglia morphology. We used the P5 mouse retina to observe microglia in both vascular and avascular areas since that microglia are associated with developing vasculature [4]. Microglia are already present in all regions of the mouse retina of mouse embryos aged 11.5 days (E11.5) [24], and angiogenesis starts at birth from the center but does not reach the retinal edges at P5 [25]. We observed 10 avascular (peripheral) and 10 vascular (around the center) areas in two retinæ (Fig. 1A).

HSI of both avascular and vascular areas are smaller than 1 (0.56 ± 0.02 vs. 0.53 ± 0.02 , respectively), indicating that the microglia distribution pattern is regular (Fig. 3 AB). The microglia density is higher in the vascular area (409 ± 11 vs. 482 ± 13 ; $P < 0.001$). The microglia thickness, including cells and processes, is higher (3.7 ± 0.5 vs. 2.0 ± 0.2 ; $P < 0.001$) and the average process length is shorter in the avascular area (9.2 ± 0.08 vs. 9.5 ± 0.1 ; $P < 0.01$), suggesting avascular (peripheral) microglia shows more amoeboid morphology. There was no significant difference in HSI, the number of processes per cell (7.4 ± 0.8 vs. 7.0 ± 0.6) and process length per cell ($68 \pm 7 \mu\text{m}$ vs. $66 \pm 5 \mu\text{m}$) between avascular and vascular areas (Fig. 3C).

Fig 3. Microglia distribution and morphology. (A) Microglia in the avascular area. (B) Microglia in the vascular area. (C) Microglia density and average process length are higher in the vascular area, while cell thickness is higher in the avascular area. There was no significant difference in HSI, the number of processes per cell, and process length per cell between vascular and avascular areas (Student's *t*-test). All data are presented as mean \pm SE.

4.2 A model of regular microglia distribution

4.2.1 Factors involved in the microglia movement model.

Since the critical factor for the observed regular microglia distribution is not clear, we listed up possible factors involved in the microglia distribution.

- **Initial distribution:** In some developmental systems, the cell arrangement pattern is regular from the beginning (like Turing patterns [26] or Delta-Notch system [27]). In the case of microglia, they migrate from the fetal yolk sac to the retina during development [13, 15] and regular spacing is reported only at a late stage of development [1]; thus, we assume that microglia initial distribution is random.
- **Random cell movement:** We observed random cell movement in microglia in organ culture (Fig. 4D). The cells show persistent random walk, which may interfere with regular cell distribution.
- **Chemotaxis toward ATP:** It is well known that ATP is a major chemoattractant of microglia [8–10], which should influence the cell distribution.
- **ATP uptake:** Pinocytosis of microglia has been reported previously [28]. We presumed that when ATP uptake by microglia is combined with ATP chemotaxis, a local decrease of chemoattractant may result in the mutual repulsion of cells [29].
- **Movement by cell-cell contact:** We hypothesized that cell-cell repulsion by direct contact plays a role in establishing the regular distribution of microglia. Although the repulsion by direct contact is not reported in microglia, some cells do repel each other by direct contact (contact inhibition of locomotion, CIL).

4.2.2 The model 159

We propose a model that includes all the factors described in the previous subsection as follows: 160
161

$$\frac{d\mathbf{r}_i}{dt} = c \nabla a|_{\mathbf{r}=\mathbf{r}_i} + k \sum_{i \neq j} f(|\mathbf{r}_j - \mathbf{r}_i|) \frac{\mathbf{r}_j - \mathbf{r}_i}{|\mathbf{r}_j - \mathbf{r}_i|} + \mathbf{v}_i \quad (2)$$

$$\frac{d\mathbf{v}_i}{dt} = \boldsymbol{\eta}(i, t) \quad (3)$$

$$\frac{\partial a}{\partial t} = p - ha - b \sum_{i=1}^n \delta(\mathbf{r}_i) + d_a \Delta a. \quad (4)$$

(2) defines the cell movement; \mathbf{r}_i represents the location of the i th microglia cell and a is the ATP distribution. c is ATP chemotactic coefficient and $f(r)$ is repulsion function (Fig. 7A). When $|\mathbf{r}_j - \mathbf{r}_i|$ is longer than repulsive radius (σ), $f(|\mathbf{r}_j - \mathbf{r}_i|) = 0$. When $|\mathbf{r}_j - \mathbf{r}_i|$ is shorter than σ , $f(|\mathbf{r}_j - \mathbf{r}_i|) = k|\mathbf{r}_j - \mathbf{r}_i|$; k is microglia repulsive strength coefficient. The function $f(r)$ mimics that microglia repel each other only when they are close. 162
163
164
165
166

(3) implements the persistent random walk. The i th cell moves at speed $v_i = |\mathbf{v}_i|$. The cell changes the direction of movement at average interval τ (persistence), which is implemented by the stochastic term $\boldsymbol{\eta}(i, t)$. 167
168
169

(4) describes the dynamics of ATP concentration; p is ATP production rate, h is ATP decay coefficient, b is ATP uptake rate, and d_a is ATP diffusion coefficient. Microglia cells move according to ATP concentration and internalize ATP (Fig. 6). ATP is generated in the whole domain (p), decay (ha) and diffuse passively ($d_a \Delta a$). 170
171
172
173

4.3 Quantification of the model parameters 174

4.3.1 Dynamics of microglial soma in organ culture 175

To quantify the dynamics of microglia, we observed microglia in the retinal organ culture. We found that microglia move randomly and appear to repel neighbors when they get closer (Fig. 4A). We tracked the microglia migration (Fig. 4B), and analyzed the tracks that are longer than 50 frames (100 min). We found that most microglia migrate a short distance ($\text{MSD} \approx 100 \mu\text{m}^2 / 100 \text{min}$, Fig. 4C). A part of the microglia migrated a long distance, which may be activated microglia because of the tissue damage by the dissection of the cultured retinas. We calculated the average of mean square displacement (MSD) 176
177
178
179
180
181
182

with passage time (Fig. 4D); the MSD showed a linear increase initially but reached a plateau after 40 min., indicating that the microglia migration area is limited.

We obtained persistent random walk parameters from the diffusion coefficient (=MSD/time) and average speed (Fig. 4). Diffusion coefficient (d_u) and average speed of the microglia (v) were $d_u = 1.9 \mu\text{m}^2/\text{min}$ and $v = 0.26 \mu\text{m}/\text{min}$ respectively. Persistence τ was calculated by $d_u/v^2 = 28.1 \text{ min}$.

Fig 4. Dynamics of microglial soma in organ culture. (A) Microglia (red circle) moving randomly and repelling surrounding other microglia (blue circles) tracked for 10 hours. White arrows represent the pairs of microglia close to each other, and gray arrows represent the pairs of microglia that move away after approaching. (B) We tracked the microglia migration inside the yellow square in the left panel for 12 hours. The right panel shows that white regions representing each cell's first position and color lines representing each cell's 12-hour trajectory. (C) The Histogram of MSD. We chose trajectories we could track for 50 frames (100 min, $n = 58$). (D) The mean MSD reached a plateau after 40 min.

4.3.2 Dynamics of microglia process formation

An obvious candidate for the cell-cell repulsion mechanism is the microglia processes. We observed the dynamics of microglia process formation using organ culture. We found the processes showed slow growth and rapid collapse (Fig. 5A-C). We measured the average growth velocity of processes g ($0.36 \pm 0.04 \mu\text{m} / \text{min}$, mean \pm SE, $n = 5$) and the collapse probability p ($0.046 \pm 0.002 / \text{min}$, mean \pm SE, $n = 10$). Based on this observation, we made a mathematical model of process distribution that predicts that microglia processes' length distribution obeys exponential distribution (Supporting Information 6.1).

The experimental results of length distribution of the fixed specimen (Fig. 3) are represented by blue dots (Fig. 5D); the relationship between the log of process number and process length is linear ($y = 7.6 - 0.14x$, $R^2 = 0.96$, avascular area vs. $y = 7.7 - 0.14x$, $R^2 = 0.97$, vascular area), which is consistent with model prediction. The values $\frac{p}{g}$ expected from the process dynamics model (0.13) are consistent with the linear fitting slope of the actual process distribution (0.14).

Additionally, we measured the nearest neighbor distance (NND) in both the avascular and the vascular areas. Minimum NND are $9.6 \mu\text{m}$ vs. $10 \mu\text{m}$, and mean NND are $32 \pm 0.3 \mu\text{m}$ vs. $30 \pm 0.2 \mu\text{m}$ in avascular and vascular areas respectively (mean \pm SE, $n = 1619$, $n = 1910$, Fig. 5E). Intuitively, microglia do not get closer beyond the average process length (9.2 ± 0.08 vs. 9.5 ± 0.1 , mean \pm SE, Fig. 3) because of the direct contact repulsion;

therefore, a minimum NND smaller than the average process length does not exist. 208

Fig 5. Dynamics of microglia process formation. (A) We obtained the kymograph of microglia process dynamics in the yellow area for 12 hours. Scale bar: 50 μm . (B) Microglia extended the process slowly and retracted quickly. (C) The process extension inclination is the yellow line, and the retraction is the red line. (D) The histogram of process distribution. (E) The histogram of NND.

4.3.3 ATP uptake, diffusion and extracellular distribution 209

We also quantified ATP dynamics in relation to microglia in mouse retina organ culture. 210

We previously reported that the lung epithelium exerted a lateral inhibitory effect on the 211 neighboring epithelium via depletion of fibroblast growth factor [29]. We presumed that 212 microglia ingest ATP, decreased the neighborhood's concentration, and keep regular 213 distribution. We observed microglia distribution and ATP concentration (Alexa 214 Fluor™647 ATP, Invitrogen Corporation, US) using the mouse retina organ culture. We 215 found ATP colocalizes with the cell body of microglia (Fig. 6A), indicating that the uptake 216 of ATP by the microglia does exist. We also measured the change in fluorescence change 217 of microglia in organ culture with 5 μM ATP-Alexa (n = 15) for 12 hours and obtained the 218 uptake rate $b = 9.5 \times 10^{-4} \mu\text{M min}^{-1}$ per microglia cell. 219

Next, we quantified the diffusion of ATP in the cultured mouse retina using FRAP. 220 Mouse P5 retina was incubated with 50 μM ATP-Alexa647 for 1 hour before the 221 experiment. The dotted circle indicates the bleach spot. From the recovery curve of the 222 fluorescence, we estimated that the diffusion coefficient of ATP is $180 \mu\text{m}^2 \text{min}^{-1}$. We 223 observed an immobile fraction in the recovery curve (Fig. 6B), indicating that the 224 diffusion of a certain compartment of ATP is very slow [30]. 225

Finally, we observed the extracellular ATP distribution and microglia using 226 ATPOS [20, 21] (Fig. 6C-E). Extracellular ATP was detected using the Cy3-Alexa488 ratio, 227 and the location of microglia was visualized using IB4-DyLight649. We could not detect a 228 decrease in extracellular ATP distribution around the microglia (Fig. 6E). 229

Fig 6. ATP dynamics in mouse retina organ culture. (A) ATP uptake of retinal microglia during 12h. Scale bar: 50 μm (B) Measurement of the ATP diffusion coefficient by FRAP. After the sample was immersed with fluorescent ATP solution, a small region of the retina was photobleached, and the recovery was observed. (C-E) The extracellular distribution of ATP. (C) Low magnification view. (D) High magnification view. (E) Fluorescence intensity ratio around microglia.

4.3.4 Model parameters

We evaluated parameter values from the experiments described above to simulate the dynamics of microglia migration and ATP concentration (Table 1). Some parameters are estimated from previous work, which is described in Supporting information (section 6.2).

Table 1. Simulation parameter values in the model

Parameter	Description	Value	Source
c	ATP chemotactic coefficient	$18 \mu\text{m}^2 \mu\text{M}^{-1} \text{min}^{-1}$	[8]
τ	Persistence	11.6 min	Fig. 4
v	Random cell migration speed	$2.5 \mu\text{m} / \text{min}$	Fig. 4
p	Extracellular ATP production rate	$1.7 * 10^{-3} \mu\text{M} \text{min}^{-1}$	Calculated from (4)
h	ATP decay coefficient	0.2min^{-1}	[31]
b	ATP uptake rate	$9.5 * 10^{-4} \mu\text{M} \text{min}^{-1} \text{microglia}^{-1}$	Fig. 6
d_a	ATP diffusion coefficient	$180 \mu\text{m}^2 \text{min}^{-1}$	Fig. 6
d_u	Microglia diffusion coefficient	$0.4 \mu\text{m}^2 \text{min}^{-1}$	[32]
σ	Microglia repulsive radius	45 μm	Fig. 5
k	Repulsive strength coefficient of discrete model	0.1min^{-1}	Determined by simulation
a_w	ATP concentration at wound site	31 μM	Determined by simulation

4.4 The numerical simulations of the model

We numerically confirmed whether the parameter set we obtained is sufficient to generate regular spacing.

Fig 7. The model simulations. (A) Determination of k . (B) Effect of chemotactic coefficient c when $k = 0$. (C) Distribution of ATP at the wound site in the model. (D) Accumulation of microglia at the wound site in the model. (E) Distribution of ATP in the normal tissue in the model. (F) Microglia distribution of the quantitative model.

Among the model parameters, the repulsion strength coefficient k is the only parameter that the experimental observation cannot determine. We numerically obtained the effect of the different k to the regular distribution of the microglia cells. k works very efficiently in terms of the regular pattern formation, and small parameters like $k = 0.1$ can generate a regular pattern (Fig. 7A). k represents the inverse of the time required for the repulsion to take effect. At first, we assumed that the depletion of ATP could also play a role, but $k = 0$ simulation shows no regular distribution, indicating the effect of direct cell-cell repulsion may be the primary factor.

One concern about the parameter estimation and ATP effect is that the chemotactic coefficient c may be underestimated because it is based on an in vitro experiment [8]. To rule out this possibility, we first observed what c value can reproduce regular spacing without cell-cell repulsion ($k = 0$). We needed a very large chemotactic factor for the

regular spacing ($c = 20000$) from the model simulation, which is 1000 times higher than
the observed value. In addition, the original model parameter ($c = 18$) reproduced the
accumulation of the microglia cells at the wounded site (Fig. 1B). Since the production
rate of the ATP at the wound site is unknown, we set the concentration of the ATP at the
wound site as the 1/1000 of the intracellular concentration (Fig. 7c, [33]). We observed the
accumulation of the microglia cells at the wound site (Fig. 7D, red), indicating that the
chemotactic coefficient c is appropriate. The final ATP distribution and microglia cell
distribution are shown in Fig. 7 EF. We observed the decrease of ATP concentration at the
microglia location, but the concentration decrease is very small (Fig. 7E), consistent with
ATPOS observation (Fig. 6C-E).

4.5 Screening molecular pathways for cell-cell interaction

Finally, we tried to specify the molecular pathway responsible for the direct contact
repulsion or ATP. Since the mechanism of repulsion by cell-cell contact has not been
described in microglia, we screened three pathways responsible for CIL: the ephrin-Eph
pathway, the Wnt-planar cell polarity (PCP) pathway, and the Semaphorin pathway.

We confirmed Eph-ephrin, Wnt-PCP, and semaphorin pathway gene are expressed in
mouse microglia using RefEx (Reference Expression dataset) [34]. We used
phosphatidylinositol-specific phospholipase C (PI-PLC) which inhibits the EphA-ephrinA
system, Secreted Frizzled Related Protein 1 (sFRP1) to block the Wnt-PCP pathway [35],
and Plexin-D1 Fc fragment to inhibit the semaphorin pathway.

We observed microglia distributions at $400 \mu\text{m} \times 400 \mu\text{m}$ in the avascular area of
organ culture for 12 hours (Fig. 8A), treated with PI-PLC, sFRP1, and Plexin-D1 Fc
fragment assumed to inhibit microglia cell-cell repulsion. THE HSI of the treated groups
tends to be higher than the control (Fig. 8B), indicating that inhibitors of cell-cell
repulsion interfere with regular microglia distribution. Microglia densities of the treated
groups are lower than the control (Fig. 8C). We assume that microglia migrate at ease
because of a lack of surrounding repulsion; thus, individual microglia migrate freely and
into the peripheral damaged area. Therefore the cell density decreases within the
observed field.

Besides, we observed the microglia distribution treated with a saturating

concentration of ATP-Alexa and clopidogrel (ATP P2Y receptor antagonist). The HSI of 279
treated groups tends to be similar to that of the control group (Fig. 8D). Microglia 280
densities of treated groups are higher than control (Fig. 8E). We assume that saturating 281
amount of ATP or ATP inhibitor mask ATP gradient from the peripheral damaged area to 282
the center of observed tissue; thus, treated microglia stay in the same position. 283

Fig 8. HSI and cell densities of microglia in organ culture. (A) $400\ \mu\text{m} \times 400\ \mu\text{m}$ 284
areas were measured. (B) HSI of the repulsion assay (control: $n = 7$, PI-PLC: $n = 5$, sFRP: 285
 $n = 5$, PlexinD1Fc: $n = 4$). (C) Cell densities of the repulsion assay. (D) HSI of the ATP 286
assay (control: $n = 7$, ATP: $n = 8$, Clopidogrel: $n = 7$). (E) Cell densities of the ATP assay. 287
All data are represented as mean \pm SE. *: one-way ANOVA, $P < 0.05$. 288

5 Discussion 284

5.1 The biological meaning of regular distribution 285

The physiological meaning of the regular distribution is not clear. The structure of resting 286
microglia serves an immune surveillance function [7]. The regular distribution is assumed 287
to be essential for the immune system and enables microglia to reach the injured site. 288

The regular distribution of microglia may play a role in the pattern formation of blood 289
vessels. It is known that microglia influences angiogenesis [36,37]. Reduced number of 290
microglia results in reduced vessel branching and density, while patterning was restored 291
by intravitreal injection of exogenous microglia [38–40]. 292

5.2 Models of microglia cell distribution 293

There are several theoretical studies concerning the distribution of microglia. Numahara 294
et al. reported that the distribution of epidermal Langerhans cells is completely regular; 295
the pattern of Voronoi divisions fits the territories hypothesized for the 296
immuno-surveillance. They estimated a repulsive interaction between the Langerhans 297
cells using the mathematical model [41]. However, the mechanism of the regular 298
distribution of Langerhans cells is not specified. 299

Another model concentrates on aggregation formation of microglia around 300
amyloid-beta plaques, not regular spacing [42]. In this work, aggregation of microglia was 301
reproduced using the Kelle-Segel type chemotaxis model [43]. 302

5.3 Microglia process dynamics

Several features are known about the dynamics of process formation. Resting microglia extends the process to the injured site [7] which is mediated by Gi-coupled P2Y₁₂ ATP receptor and downstream Rac GTPase-driven actin polymerization [8]. Process retraction during the transition from resting to active microglia is mediated by the adenosine A_{2A} receptor [44]. The speed of process extension and retraction were similar in the brain [7], which is different from our observation in the retina (Fig. 5 C). Resting microglia process movement is interspersed with a brief static period. The physiological meaning of this fixed period is not clear [7].

We investigated the dynamics of the microglia process formation to obtain the characteristic length of repulsion. The mathematical model contains an advection term, representing constant growth of the processes, and degradation term, which represents the probabilistic process collapse. This model fits the experimentally observed process length distribution. This model is similar to our previous model [45] and essentially equivalent to the McKendrick-von Forester equation with a uniform death rate [46]. We found that microglia do not get closer beyond the average process length. We presume that microglia maintain distances between other microglia while extending and retracting the processes.

5.4 Contact Inhibition of Locomotion pathway

To our knowledge, there is no previous report describing the mechanism of microglia repulsion via contact by processes. Therefore we examined a general cell repulsion mechanism known as the contact inhibition of locomotion, initially described in the behavior of fibroblast cells [47, 48].

Three molecular pathways of CIL are known - the Eph-ephrin pathway [49], the Wnt-PCP pathway [49, 50] and the Semaphorin pathway [51]. Eph and ephrin are membrane-bound receptors and ligands, respectively, and when Eph-expressing cells contact an ephrin-expressing cell, the cells repel each other. Ephrin-Eph signaling plays an essential role in cell segregation during development [52, 53]. Noncanonical Wnts (e.g., Wnt4, Wnt5A, and Wnt11) activate PCP [54] that is related to CIL. sFRP is one of the extracellular inhibitors of this pathway [35]. Semaphorins are secreted or

transmembrane proteins that mediate repulsive axon guidance, immune cell regulation, 333
and vascular growth and remodeling [55]. Semaphorins signal through plexins that 334
recruit and regulate kinases and Rho-family GTPases to control cell motility [56]. 335

5.5 Cell-cell repulsion by direct contact in other systems 336

Although the mechanism of cell-cell repulsion in microglia has not been reported, previous 337
works described the mechanism in other cell types. Mouse oligodendrocyte precursor cells 338
(OPC) survey their local environment with motile filopodia and maintain unique 339
territories through self-avoidance [57]. In *Drosophila* da sensory neurons, the mutual 340
repulsion of dendrites is regulated by gene encoded in Dscam (Down syndrome cell 341
adhesion molecule) locus [58]. PVD nociceptive neuron in *C. elegans* extends dendrites 342
that do not cross each other. The axon guidance protein UNC-6/Netrin is required for this 343
self-avoidance [59]. Two mouse retinal interneuron subtypes (starburst amacrine cells 344
and horizontal cells) show regular distribution, and MEGF10 and MEGF11 are involved 345
in this regular distribution [60]. 346

6 Supporting information 347

6.1 Model of microglia process length distribution 348

Based on the experimentally observed motion of the process, we modeled the dynamics of process length distribution $u(x, t)$ using advection and degradation terms as follows: 349
350

$$\frac{\partial}{\partial t} u(x, t) = -g \frac{\partial}{\partial x} u(x, t) - p u(x, t). \quad (5)$$

g is the velocity of process extension and p is the collapse probability of process. By the model (5), the steady-state of length distribution $u(x, \infty)$ can be described as follows: 351
352

$$u(x, \infty) = U_0 e^{-\frac{p}{g} x}. \quad (6)$$

U_0 represents $u(0, \infty)$, the steady-state length distribution of the microglia process. U_0 is exponential distribution, indicating there is a linear relationship between the log of process number and process length. 353
354
355

The sum of the process length is described by the definite integral as follows: 356

$$\int_0^{\infty} x u(x, \infty) dx = \int_0^{\infty} x U_0 e^{-\frac{p}{g} x} dx = U_0 \frac{g^2}{p^2}. \quad (7)$$

U_0 in avascular are (7.6) and vascular areas (7.7) are obtained by linear fitting equation. $U_0 \frac{g^2}{p^2}$ are $1.0 \times 10^5 \mu\text{m}$ vs. $1.1 \times 10^5 \mu\text{m}$, and the sum of the process length from experimental results are $1.1 \times 10^5 \mu\text{m}$ vs. $1.3 \times 10^5 \mu\text{m}$, respectively. The model captures the characteristics of the actual process distribution. 357
358
359
360

6.2 Obtaining simulation parameters from previous literatures 361

- c : We calculated the ATP chemotaxis coefficient using the published data of ATP chemotaxis of microglia in the Dunn chamber [8]. 362
363
- h : We determined the ATP decay coefficient by fitting the data that ATP decay of homogenized retina [31]. The fitting equation as follows:

$$a(t) = c_0 + c_1 t + c_2 e^{-ht} \quad (c_n : \text{constant}). \quad (8)$$

- p : The basal extracellular ATP production rate [61] is calculated by steady state concentration of ATP (a_0) and ATP decay rate h . We used extracellular ATP of the bovine retina (6.2 ± 0.7 nM [62]) as a_0 . We obtain p by steady state equilibrium $0 = p - ha_0$. Uptake by microglia is small and neglected in this calculation.
- σ : Davis *et al.* reported the exclusion radii (58.6 ± 1.4 μm) and the average NND (40 ± 1.0 μm) in adult mouse retina [17]. We measured the average NND (31 ± 0.12 μm , $n = 7053$, Fig. 3) in P5 mouse retina; thus, we assumed microglia repulsion radius is 45 μm , considering the ratio of their report [17].
- a_w : Intracellular ATP is millimolar order [33]. We set production of ATP at the wound site so that a_w becomes 1/1000 of intracellular ATP.

365

366

367

368

369

370

371

372

373

374

7 Acknowledgments

375

This work is financially supported by JSPS KAKENHI (Grant Nos. 20H03427 to Kenzo Hirose, and 20H02875 to Daisuke Asanuma). The authors would like to thank Shuji Ishihara (University of Tokyo) for discussions and comments, and Enago (www.enago.jp) for the English language review.

376

377

378

379

References

1. Hume DA, Perry VH, Gordon S. Immunohistochemical localization of a macrophage-specific antigen in developing mouse retina: phagocytosis of dying neurons and differentiation of microglial cells to form a regular array in the plexiform layers. *Journal of Cell Biology*. 1983;97(1):253–257. doi:10.1083/jcb.97.1.253.
2. Konishi H, Kiyama H, Ueno M. Dual functions of microglia in the formation and refinement of neural circuits during development. *International Journal of Developmental Neuroscience*. 2018;doi:10.1016/j.ijdevneu.2018.09.009.

3. Hattori Y, Naito Y, Tsugawa Y, Nonaka S, Wake H, Nagasawa T, et al. Transient microglial absence assists postmigratory cortical neurons in proper differentiation. *Nature Communications*. 2020;11(1):1631. doi:10.1038/s41467-020-15409-3.
4. Fantin A, Vieira JM, Gestri G, Denti L, Schwarz Q, Prykhodzhiy S, et al. Tissue macrophages act as cellular chaperones for vascular anastomosis downstream of VEGF-mediated endothelial tip cell induction. *Blood*. 2010;116(5):829–840. doi:10.1182/blood-2009-12-257832.
5. Kreutzberg GW. Microglia: A sensor for pathological events in the CNS. *Trends in Neurosciences*. 1996;19(8):312–318. doi:10.1016/0166-2236(96)10049-7.
6. Kierdorf K, Prinz M. Factors regulating microglia activation. *Frontiers in Cellular Neuroscience*. 2013;7(April):1–8. doi:10.3389/fncel.2013.00044.
7. Nimmerjahn A, Kirchhoff F, Helmchen F. Resting microglial cells are highly dynamic surveillants of brain parenchyma in vivo. *Neuroforum*. 2005;11(3):95–96. doi:10.1515/nf-2005-0304.
8. Honda S, Sasaki Y, Ohsawa K, Imai Y, Nakamura Y, Inoue K, et al. Extracellular ATP or ADP Induce Chemotaxis of Cultured Microglia through G_{i/o}-Coupled P2Y Receptors. *The Journal of Neuroscience*. 2001;21(6):1975–1982. doi:10.1523/JNEUROSCI.21-06-01975.2001.
9. Sasaki Y, Hoshi M, Akazawa C, Nakamura Y, Tsuzuki H, Inoue K, et al. Selective expression of G_{i/o}-coupled ATP receptor P2Y₁₂ in microglia in rat brain. *Glia*. 2003;44(3):242–250. doi:10.1002/glia.10293.
10. Madry C, Attwell D. Receptors, ion channels, and signaling mechanisms underlying Microglial dynamics. *Journal of Biological Chemistry*. 2015;290(20):12443–12450. doi:10.1074/jbc.R115.637157.
11. Davalos D, Grutzendler J, Yang G, Kim JV, Zuo Y, Jung S, et al. ATP mediates rapid microglial response to local brain injury in vivo. *Nature Neuroscience*. 2005;8(6):752–758. doi:10.1038/nn1472.

12. Ginhoux F, Greter M, Leboeuf M, Nandi S, See P, Gokhan S, et al. Fate Mapping Analysis Reveals That Adult Microglia Derive from Primitive Macrophage. *Science*. 2010;701(November):841–845. doi:10.1126/science.1194637.
13. Fan Y, Xie L, Chung CY. Signaling Pathways Controlling Microglia Chemotaxis. *Molecules and Cells*. 2017;40(3):163–168. doi:10.14348/molcells.2017.0011.
14. Helmut K, Hanisch UK, Noda M, Verkhratsky A. Physiology of microglia. *Physiological Reviews*. 2011;91(2):461–553. doi:10.1152/physrev.00011.2010.
15. Martín-Estebané M, Navascués J, Sierra-Martín A, Martín-Guerrero SM, Cuadros MA, Carrasco MC, et al. Onset of microglial entry into developing quail retina coincides with increased expression of active caspase-3 and is mediated by extracellular ATP and UDP. *PLOS ONE*. 2017;12(8):e0182450. doi:10.1371/journal.pone.0182450.
16. Gomez Perdiguero E, Klapproth K, Schulz C, Busch K, Azzoni E, Crozet L, et al. Tissue-resident macrophages originate from yolk-sac-derived erythro-myeloid progenitors. *Nature*. 2015;518(7540):547–551. doi:10.1038/nature13989.
17. Davis BM, Salinas-Navarro M, Cordeiro MF, Moons L, Groef LD. Characterizing microglia activation: A spatial statistics approach to maximize information extraction. *Scientific Reports*. 2017;7(1):1–12. doi:10.1038/s41598-017-01747-8.
18. Kubota Y, Takubo K, Hirashima M, Nagoshi N, Kishi K, Okuno Y, et al. Isolation and function of mouse tissue resident vascular precursors marked by myelin protein zero. *The Journal of Experimental Medicine*. 2011;208(5):949–960. doi:10.1084/jem.20102187.
19. Kang M, Day CA, Kenworthy AK, DiBenedetto E. Simplified Equation to Extract Diffusion Coefficients from Confocal FRAP Data. *Traffic*. 2012;13(12):1589–1600. doi:10.1111/tra.12008.
20. Kitajima N, Takikawa K, Sekiya H, Satoh K, Asanuma D, Sakamoto H, et al. Real-time in vivo imaging of extracellular ATP in the brain with a hybrid-type fluorescent sensor. *eLife*. 2020;9:1–18. doi:10.7554/eLife.57544.

21. Kitajima N, Takikawa K, Sekiya H, Asanuma D, Sakamoto H, Namiki S, et al. In vivo Fluorescence Imaging of Extracellular ATP in the Mouse Cerebral Cortex with a Hybrid-type Optical Sensor. *BIO-PROTOCOL*. 2021;11(11):1–16.
doi:10.21769/BioProtoc.4046.
22. Schindelin J, Arganda-Carreras I, Frise E. Fiji: An open-source platform for biological-image analysis. *Nature Methods*. 2012;9(7):676–682.
doi:10.1038/nmeth.2019.
23. HOPKINS B, SKELLAM JG. A New Method for determining the Type of Distribution of Plant Individuals. *Annals of Botany*. 1954;18(2):213–227.
doi:10.1093/oxfordjournals.aob.a083391.
24. Santos AM, Calvente R, Tassi M. Embryonic and postnatal development of microglial cells in the mouse retina. *The Journal of Comparative Neurology*. 2008;506(2):224–239. doi:10.1002/cne.21538.
25. Stahl A, Connor KM, Sapielha P, Chen J, Dennison RJ, Krah NM, et al. The Mouse Retina as an Angiogenesis Model. *Investigative Ophthalmology and Visual Science*. 2010;51(6):2813. doi:10.1167/iovs.10-5176.
26. Kondo S, Miura T. Reaction-Diffusion Model as a Framework for Understanding Biological Pattern Formation. *Science*. 2010;329(5999):1616–1620.
doi:10.1126/science.1179047.
27. Collier JR, Monk NAM, Maini PK, Lewis JH. Pattern Formation by Lateral Inhibition with Feedback: a Mathematical Model of Delta-Notch Intercellular Signalling. *Journal of Theoretical Biology*. 1996;183(4):429–446.
doi:10.1006/jtbi.1996.0233.
28. Li Hq, Chen C, Dou Y, Wu Hj, Liu Yj, Lou HF, et al. P2Y4 Receptor-Mediated Pinocytosis Contributes to Amyloid Beta-Induced Self-Uptake by Microglia. *Molecular and Cellular Biology*. 2013;33(21):4282–4293.
doi:10.1128/MCB.00544-13.

29. Miura T, Shiota K. Depletion of FGF acts as a lateral inhibitory factor in lung branching morphogenesis in vitro. *Mechanisms of Development*. 2002;116(1-2):29–38. doi:10.1016/S0925-4773(02)00132-6.
30. Kang M, Day CA, Kenworthy AK, DiBenedetto E. Simplified Equation to Extract Diffusion Coefficients from Confocal FRAP Data. *Traffic*. 2012;13(12):1589–1600. doi:10.1111/tra.12008.
31. Winkler BS. Relative inhibitory effects of ATP depletion, ouabain and calcium on retinal photoreceptors. *Experimental Eye Research*. 1983;36(4):581–594. doi:10.1016/0014-4835(83)90052-0.
32. Juliano J, Gil O, Hawkins-Daarud A, Noticewala S, Rockne RC, Gallaher J, et al. Comparative dynamics of microglial and glioma cell motility at the infiltrative margin of brain tumours. *Journal of the Royal Society Interface*. 2018;15(139). doi:10.1098/rsif.2017.0582.
33. Imamura H, Huynh Nhat KP, Togawa H, Saito K, Iino R, Kato-Yamada Y, et al. Visualization of ATP levels inside single living cells with fluorescence resonance energy transfer-based genetically encoded indicators. *Proceedings of the National Academy of Sciences*. 2009;106(37):15651–15656. doi:10.1073/pnas.0904764106.
34. Ono H, Ogasawara O, Okubo K, Bono H. RefEx, a reference gene expression dataset as a web tool for the functional analysis of genes. *Scientific Data*. 2017;4. doi:10.1038/sdata.2017.105.
35. Kawano Y, Kypta R. Secreted antagonists of the Wnt signalling pathway. *Journal of Cell Science*. 2003;116(13):2627 LP – 2634. doi:10.1242/jcs.00623.
36. Penfold PL, Provis JM, Madigan MC, van Driel D, Billson FA. Angiogenesis in normal human retinal development the involvement of astrocytes and macrophages. *Graefe's Archive for Clinical and Experimental Ophthalmology*. 1990;228(3):255–263. doi:10.1007/BF00920031.
37. Chen S, Tisch N, Kegel M, Yerbes R, Hermann R, Hudalla H, et al. CNS Macrophages Control Neurovascular Development via CD95L. *Cell Reports*. 2017;19(7):1378–1393. doi:10.1016/j.celrep.2017.04.056.

38. Checchin D, Sennlaub F, Levavasseur E, Leduc M, Chemtob S. Potential role of microglia in retinal blood vessel formation. *Investigative Ophthalmology and Visual Science*. 2006;47(8):3595–3602. doi:10.1167/iovs.05-1522.
39. Ritter MR, Banin E, Moreno SK, Aguilar E, Dorrell MI, Friedlander M. Myeloid progenitors differentiate into microglia and promote vascular repair in a model of ischemic retinopathy. *Journal of Clinical Investigation*. 2006;116(12):3266–3276. doi:10.1172/JCI29683.
40. Kubota Y, Takubo K, Shimizu T, Ohno H, Kishi K, Shibuya M, et al. M-CSF inhibition selectively targets pathological angiogenesis and lymphangiogenesis. *Journal of Experimental Medicine*. 2009;206(5):1089–1102. doi:10.1084/jem.20081605.
41. Numahara T, Tanemura M, Numahara K, Moriue J, Shirahige Y. Spatial Statistics for Epidermal Langerhans Cells — Effects of Protopic Ointment 0.1 % on the Spatial Distribution —. *Forma*. 2009;24:49–59.
42. Kinney AC, Swanson ER. Modeling Aggregation of Proliferating Microglia in Response to Amyloid-beta in Dementia. *SPORA: A Journal of Biomathematics*. 2017;3(1). doi:10.30707/SPORA3.1Kinney.
43. Keller EF, Segel LA. Model for chemotaxis. *Journal of Theoretical Biology*. 1971;30(2):225–234. doi:10.1016/0022-5193(71)90050-6.
44. Orr AG, Orr AL, Li XJ, Gross RE, Traynelis SF. Adenosine A(2A) receptor mediates microglial process retraction. *Nature neuroscience*. 2009;12(7):872–878. doi:10.1038/nn.2341.
45. Sasaki D, Nakajima H, Yamaguchi Y, Yokokawa R, Ei SI, Miura T. Mathematical modeling for meshwork formation of endothelial cells in fibrin gels. *Journal of Theoretical Biology*. 2017;429:95–104. doi:10.1016/j.jtbi.2017.06.012.
46. Keyfitz BL, Keyfitz N. The McKendrick partial differential equation and its uses in epidemiology and population study. *Mathematical and Computer Modelling*. 1997;26(6):1–9. doi:10.1016/S0895-7177(97)00165-9.

47. Abercrombie M, Heaysman JEM. Observations on the social behaviour of cells in tissue culture. *Experimental Cell Research*. 1953;5(1):111–131.
doi:10.1016/0014-4827(53)90098-6.
48. Abercrombie M, Heaysman JEM. Observations on the social behaviour of cells in tissue culture. *Experimental Cell Research*. 1954;6(2):293–306.
doi:10.1016/0014-4827(54)90176-7.
49. Roycroft A, Mayor R. Molecular basis of contact inhibition of locomotion. *Cellular and Molecular Life Sciences*. 2016;73(6):1119–1130.
doi:10.1007/s00018-015-2090-0.
50. Eszter KV, Antic D, Jeffrey DA. Planar cell polarity signaling: the developing cell's compass. *Cold Spring Harbor perspectives in biology*. 2009;1(3):1–19.
doi:10.1101/cshperspect.a002964.
51. Hung RJ, Terman JR. Extracellular inhibitors, repellents, and semaphorin/plexin/MICAL-mediated actin filament disassembly. *Cytoskeleton*. 2011;68(8):415–433. doi:10.1002/cm.20527.
52. Fagotto F, Winklbauer R, Rohani N. Ephrin-Eph signaling in embryonic tissue separation. *Cell Adhesion and Migration*. 2014;8(4):308–326.
doi:10.4161/19336918.2014.970028.
53. Nievergall E, Lackmann M, Janes PW. Eph-dependent cell-cell adhesion and segregation in development and cancer. *Cellular and Molecular Life Sciences*. 2012;69(11):1813–1842. doi:10.1007/s00018-011-0900-6.
54. Kohn AD, Moon RT. Wnt and calcium signaling: β -Catenin-independent pathways. *Cell Calcium*. 2005;38(3-4):439–446. doi:10.1016/J.CECA.2005.06.022.
55. Alto LT, Terman JR. Semaphorins and their Signaling Mechanisms. In: *Methods in molecular biology* (Clifton, N.J.). vol. 1493. Springer; 2017. p. 1–25. Available from: http://link.springer.com/10.1007/978-1-4939-6448-2_1.
56. Kruger RP, Aurandt J, Guan KL. Semaphorins command cells to move. *Nature Reviews Molecular Cell Biology*. 2005;6(10):789–800. doi:10.1038/nrm1740.

57. Hughes EG, Kang SH, Fukaya M, Bergles DE. Oligodendrocyte progenitors balance growth with self-repulsion to achieve homeostasis in the adult brain. *Nature Neuroscience*. 2013;16(6):668–676. doi:10.1038/nn.3390.
58. Matthews BJ, Kim ME, Flanagan JJ, Hattori D, Clemens JC, Zipursky SL, et al. Dendrite Self-Avoidance Is Controlled by Dscam. *Cell*. 2007;129(3):593–604. doi:10.1016/j.cell.2007.04.013.
59. Smith CJ, Watson JD, VanHoven MK, Colón-Ramos DA, Miller DM. Netrin (UNC-6) mediates dendritic self-avoidance. *Nature Neuroscience*. 2012;15(5):731–737. doi:10.1038/nn.3065.
60. Kay JN, Chu MW, Sanes JR. MEGF10 and MEGF11 mediate homotypic interactions required for mosaic spacing of retinal neurons. *Nature*. 2012;483(7390):465–469. doi:10.1038/nature10877.
61. Corriden R, Insel PA. Basal Release of ATP: An Autocrine-Paracrine Mechanism for Cell Regulation. *Science Signaling*. 2010;3(104):re1–re1. doi:10.1126/scisignal.3104re1.
62. David Reigada, Wennan Lu, May Zhang CHM, Reigada D, Lu W, Zhang M, Mitchell CH. Elevated pressure triggers a physiological release of ATP from the retina: Possible role for pannexin hemichannels. *Neuroscience*. 2008;19(2):396–404. doi:10.1016/j.neuroscience.2008.08.036.

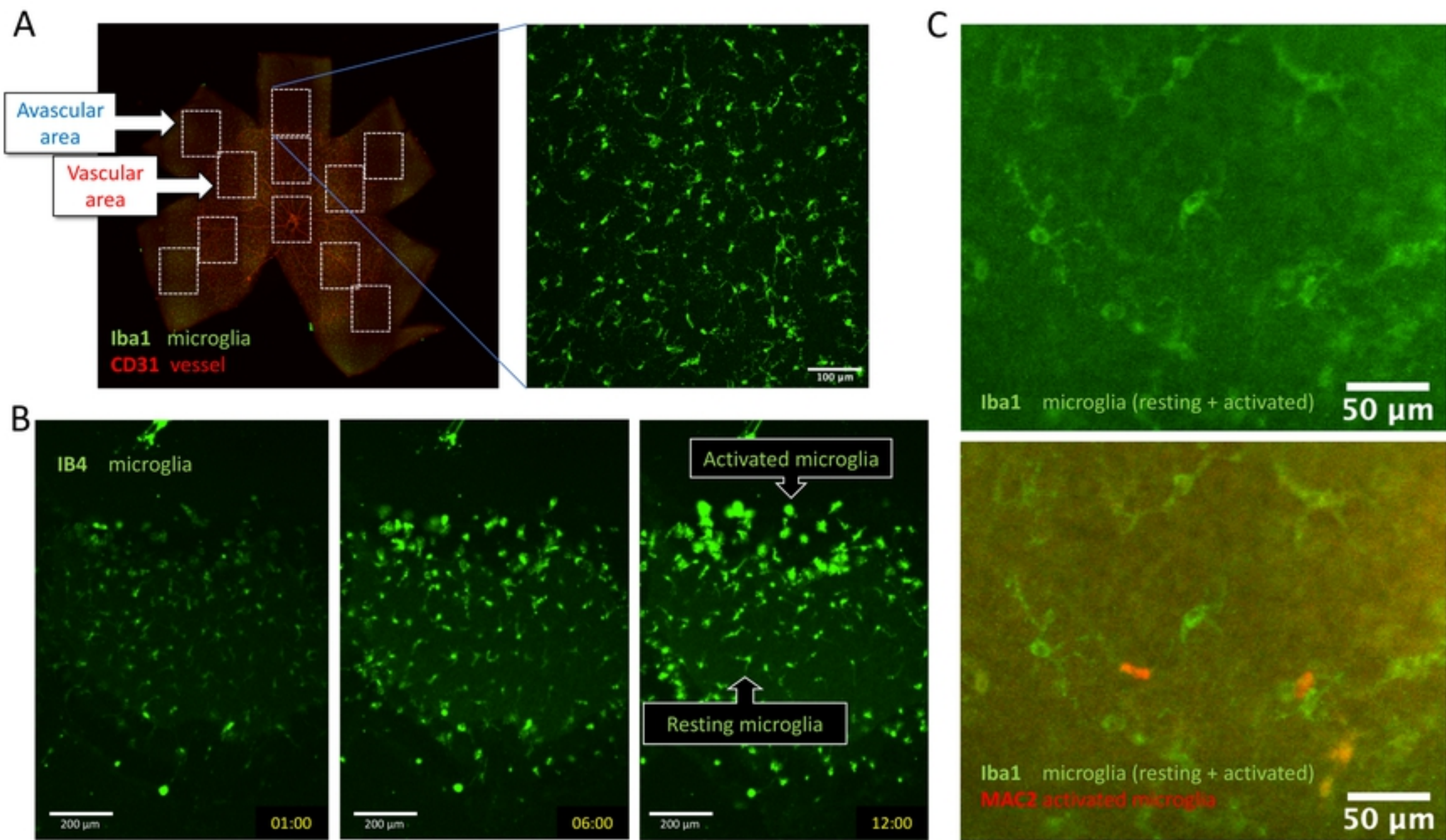


Fig1

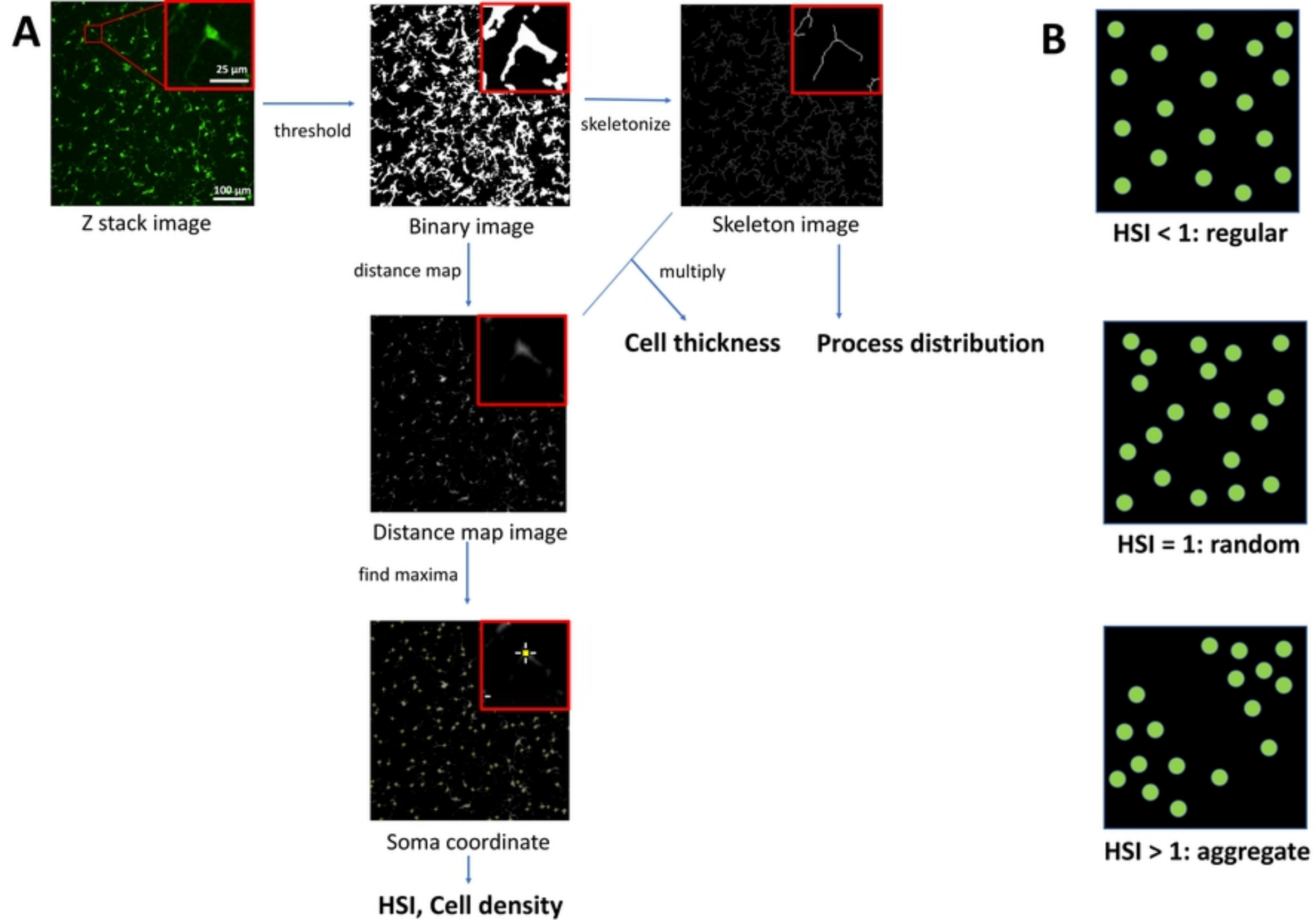


Fig2

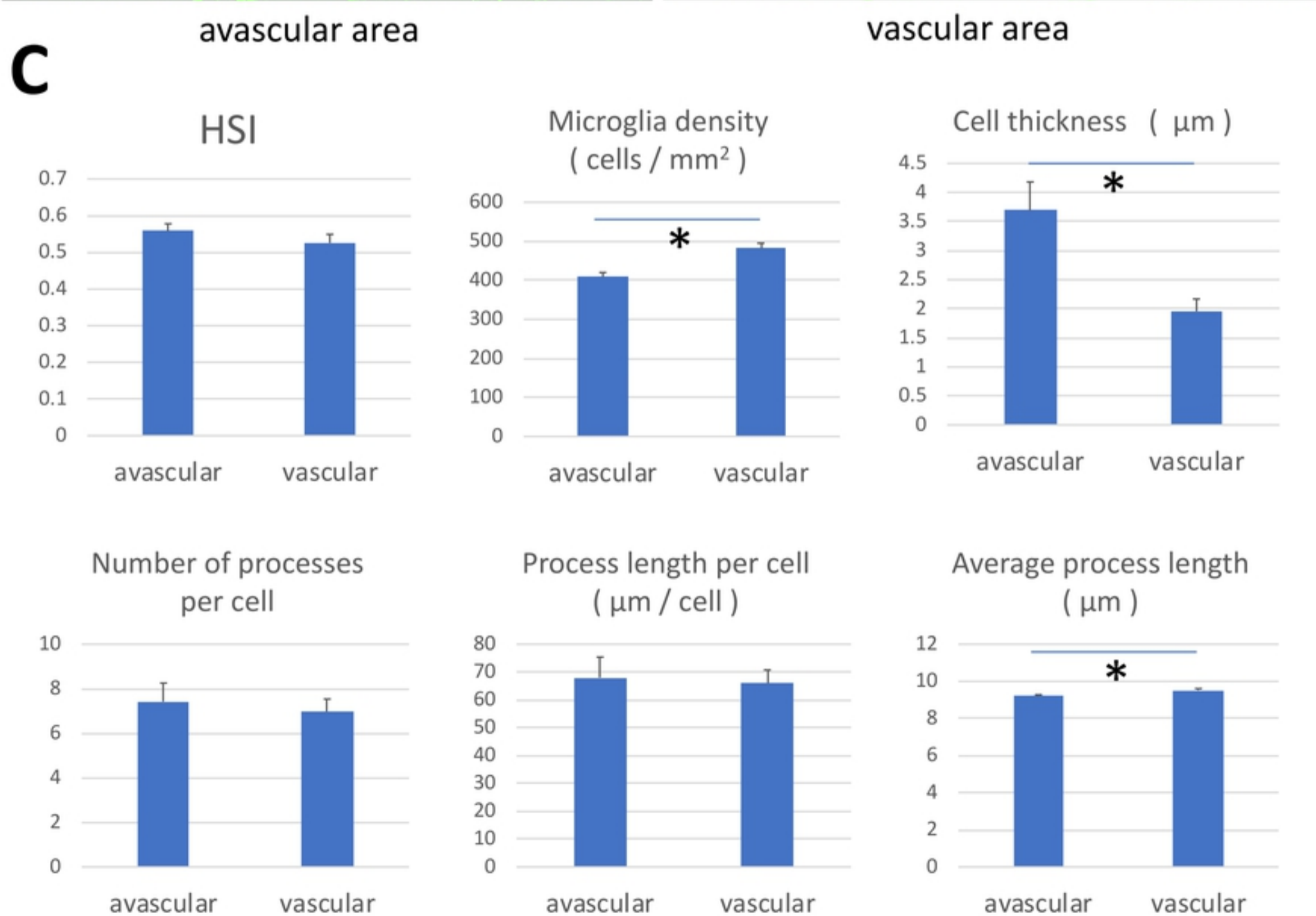
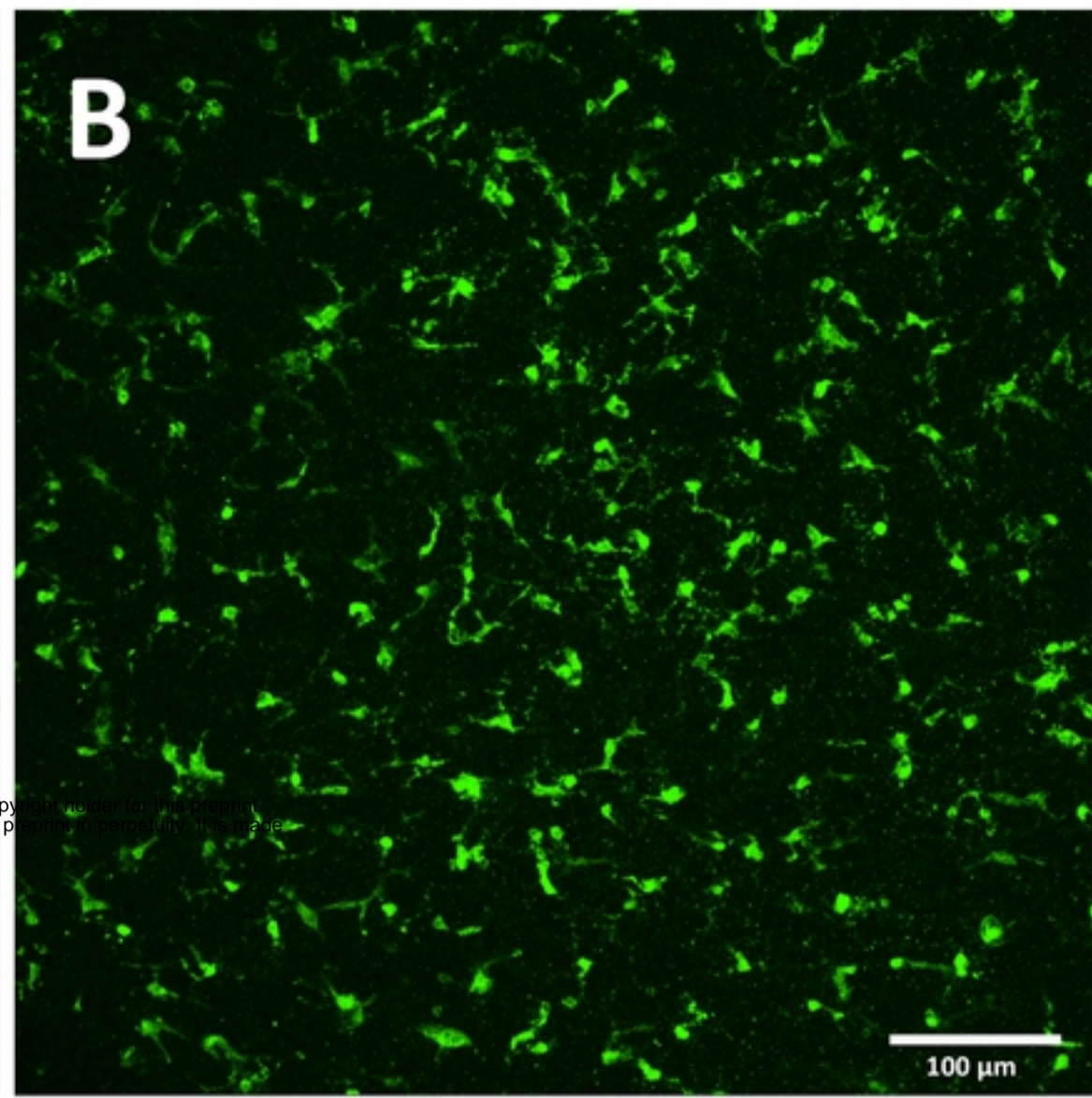
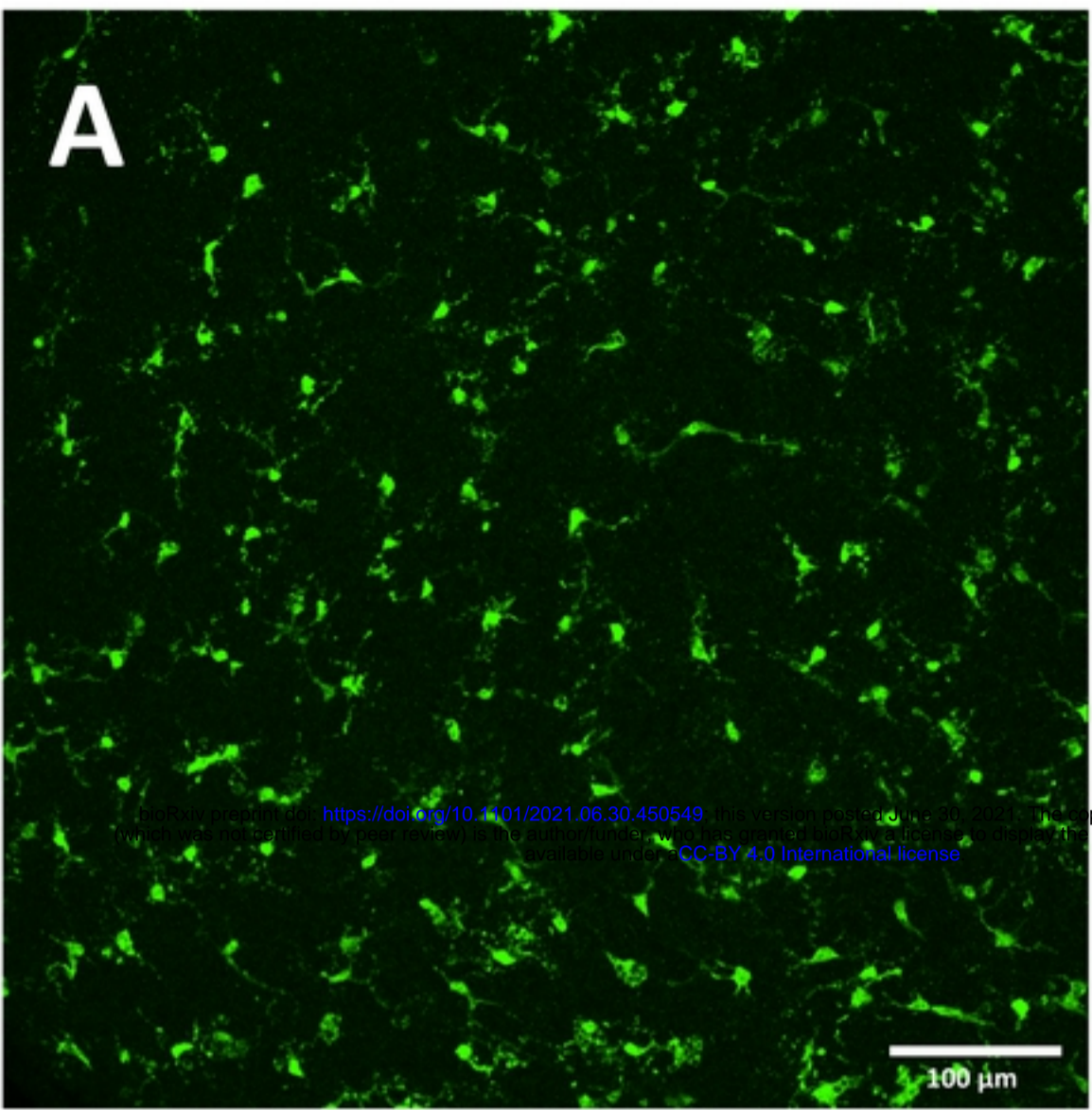


Fig3

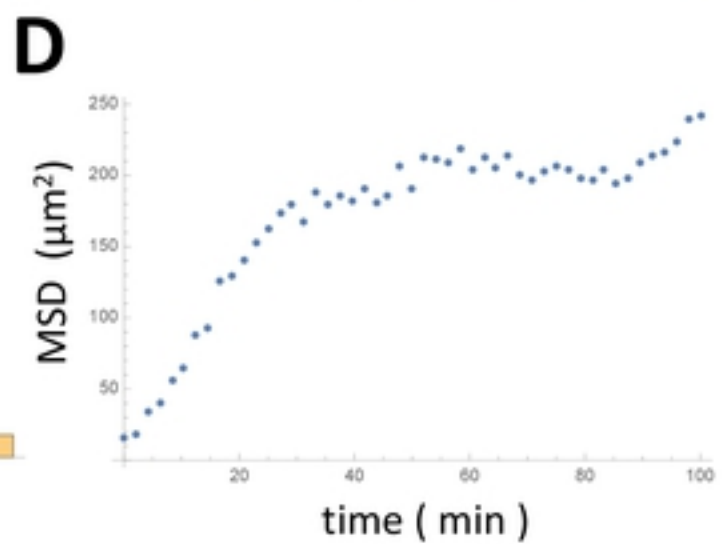
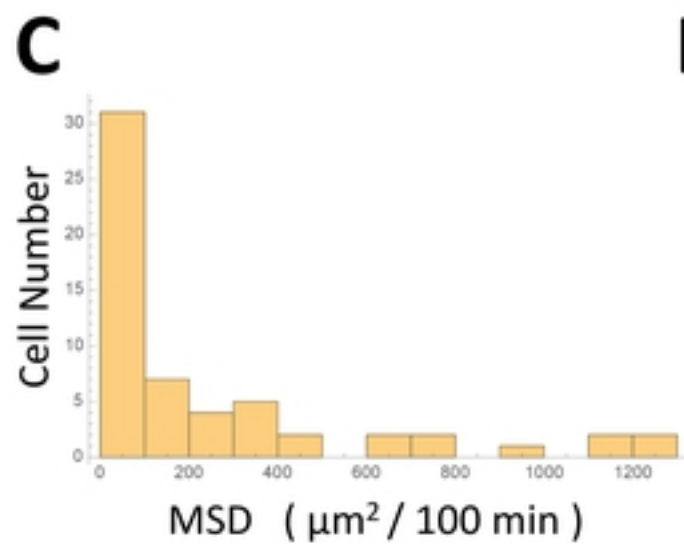
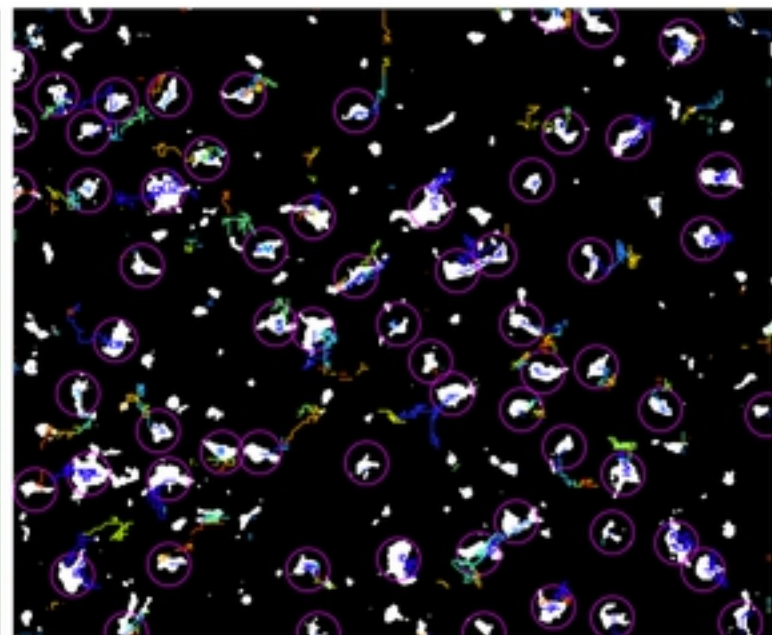
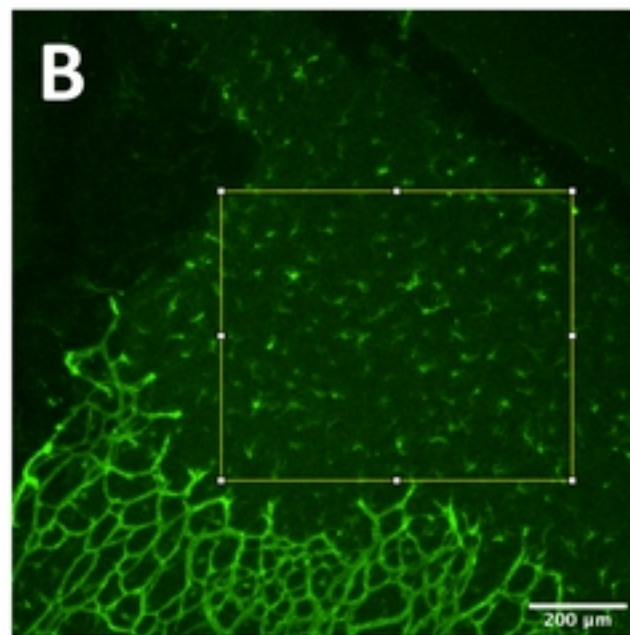
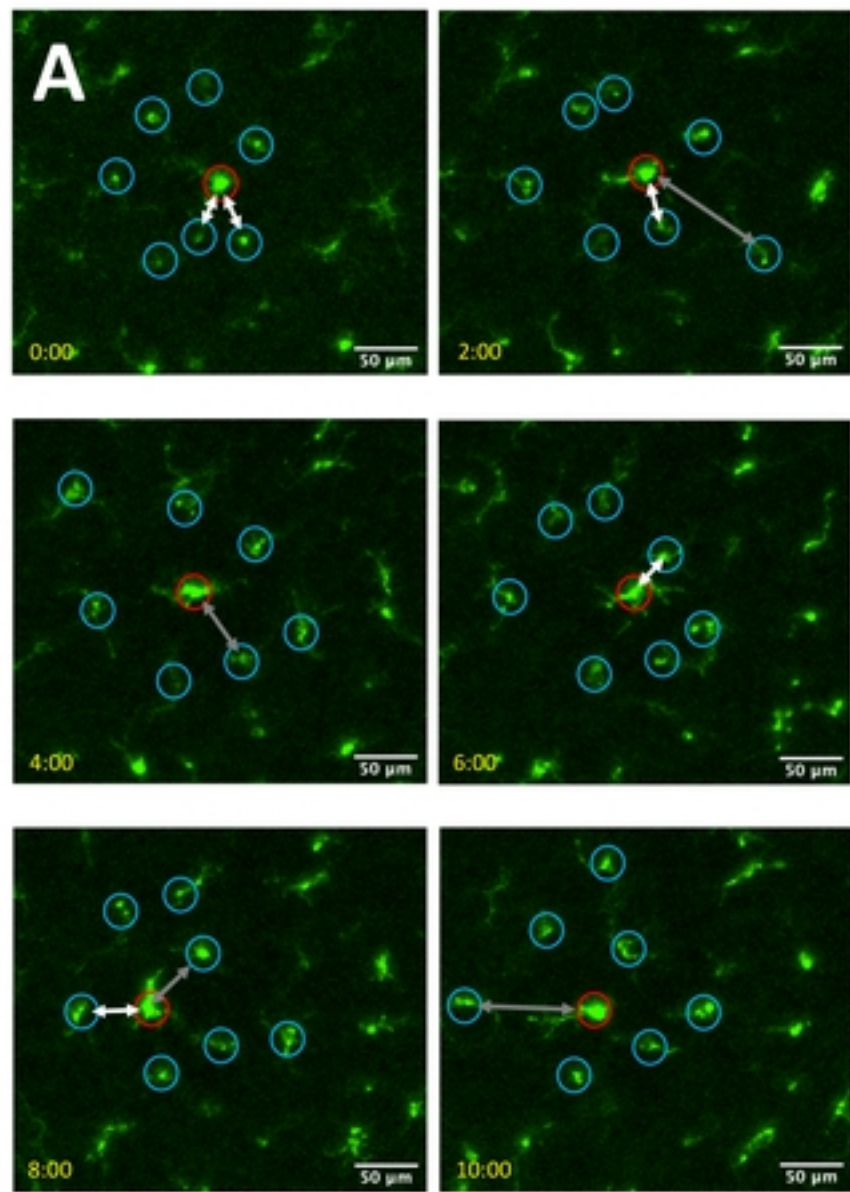


Fig4

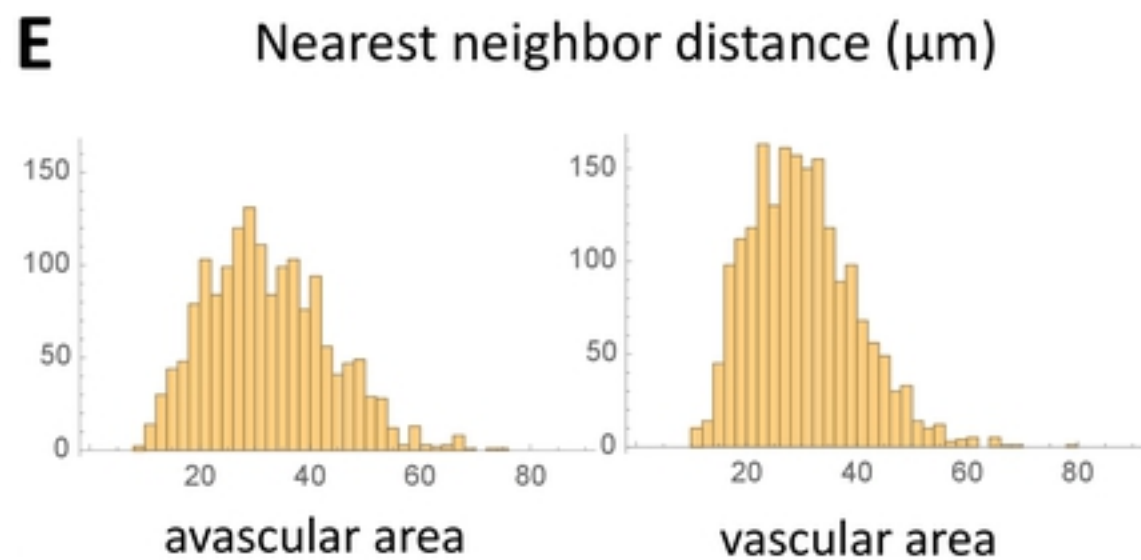
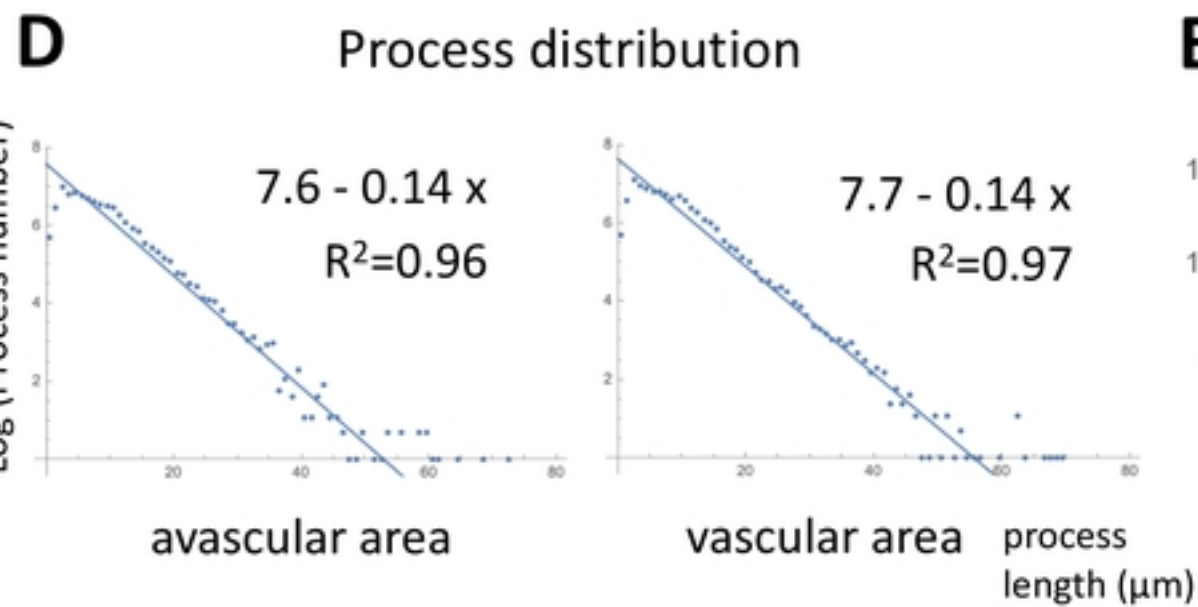
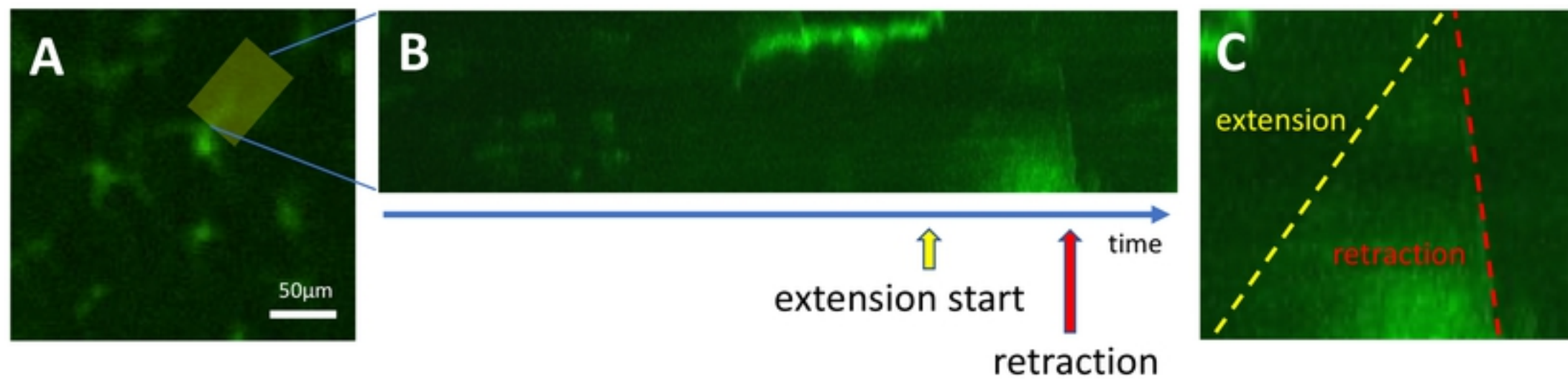


Fig5

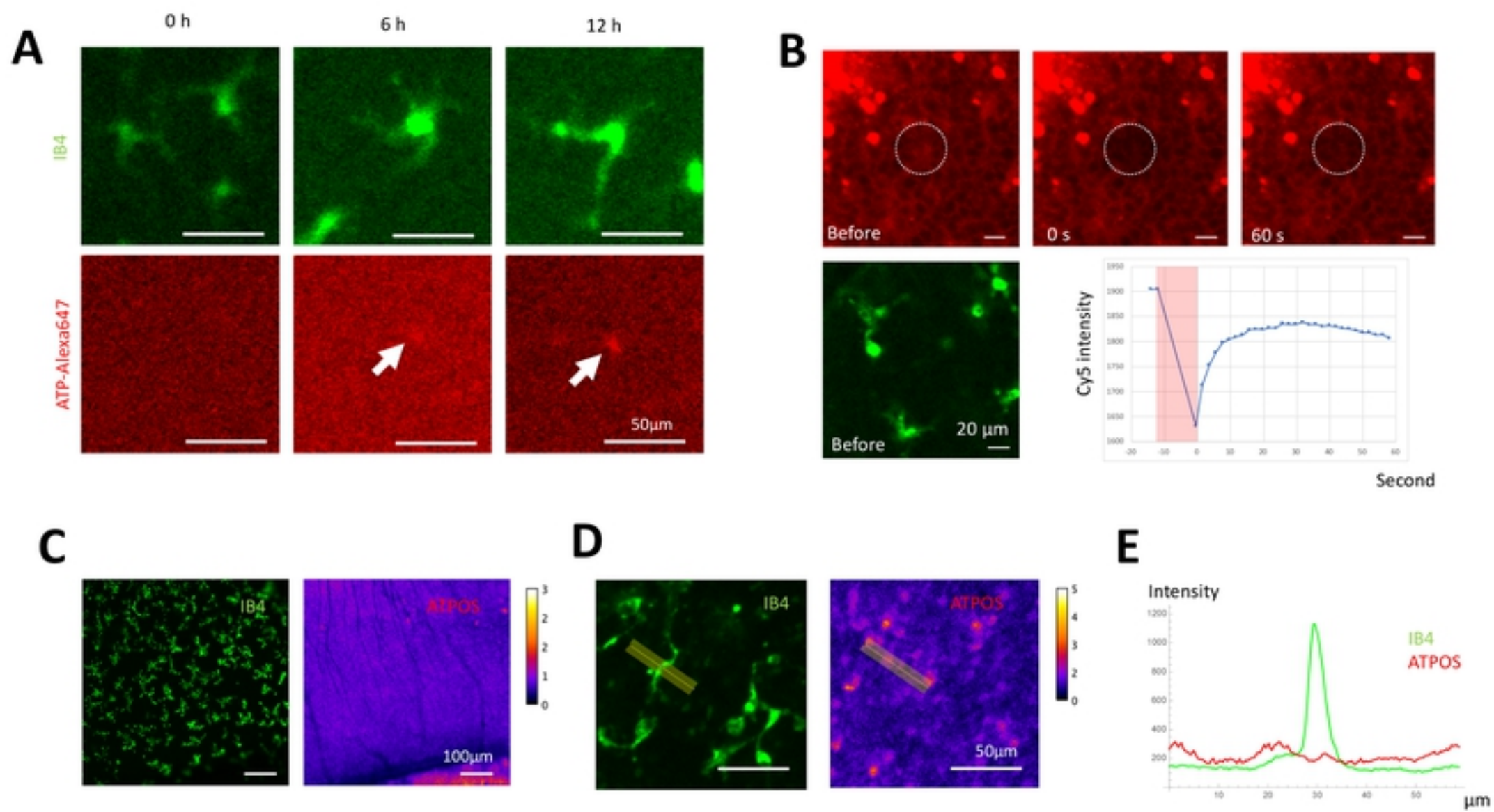


Fig6

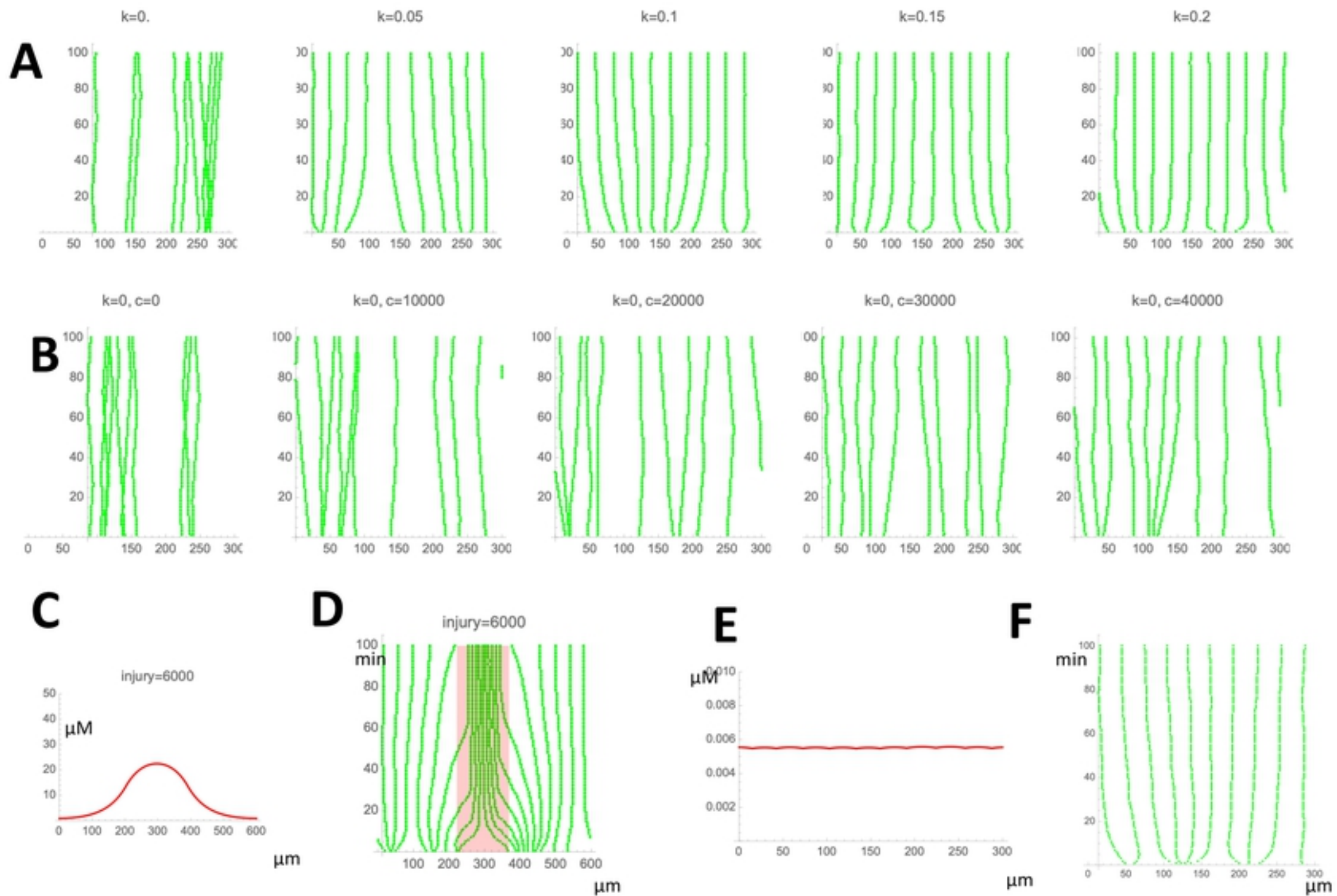


Fig7

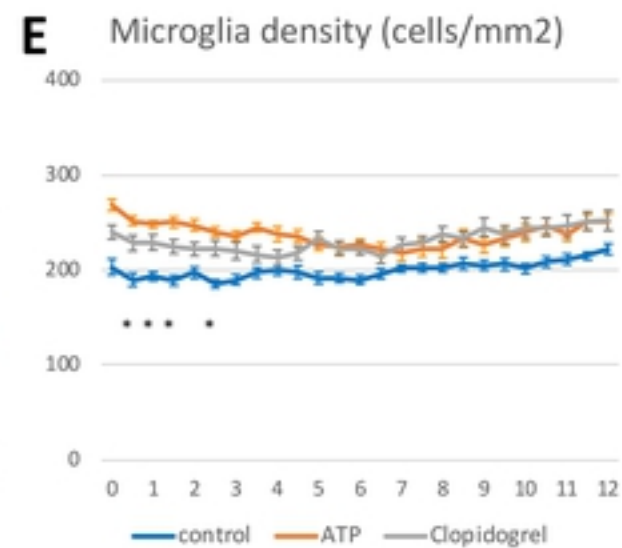
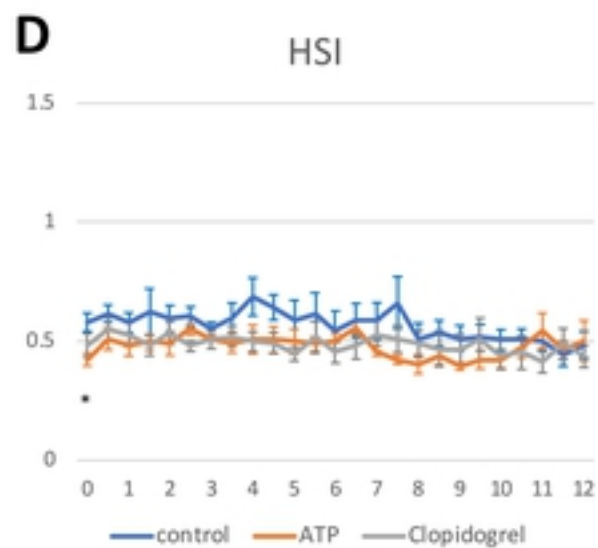
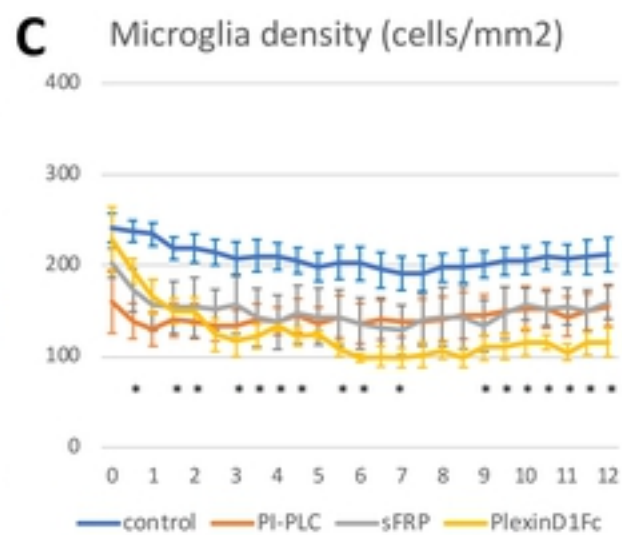
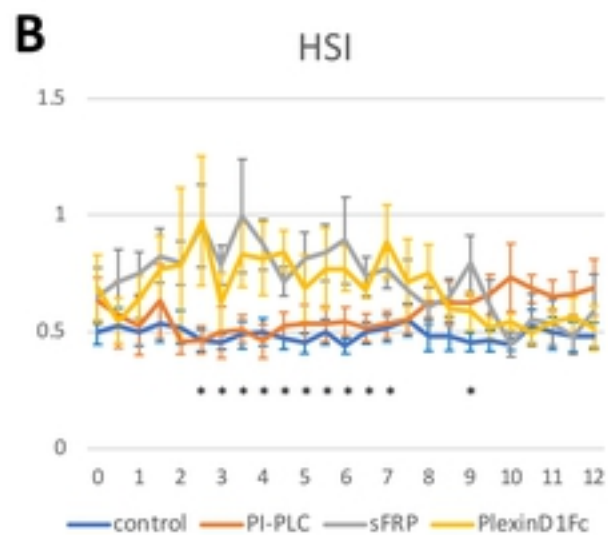
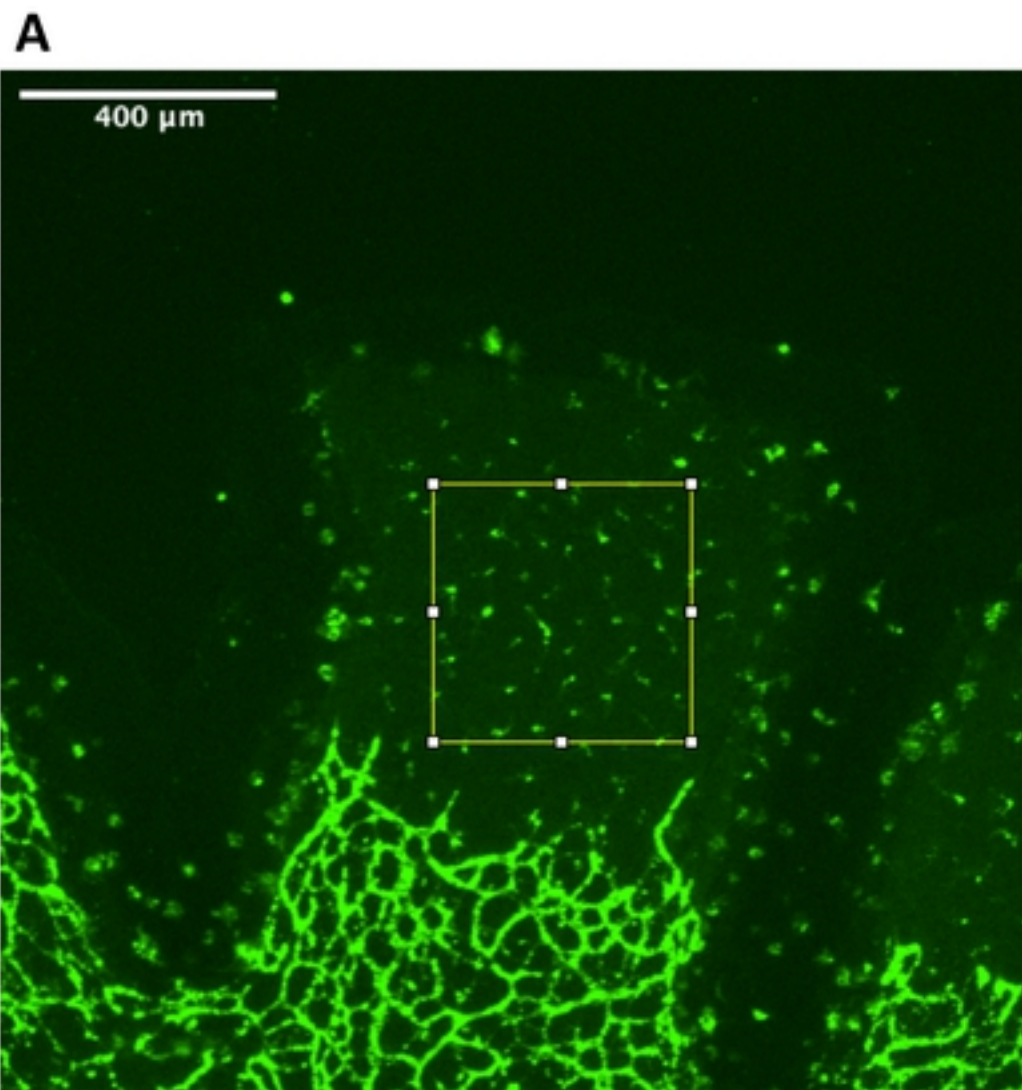


Fig8